PCCP

Accepted Manuscript

ROYAL SOCIETY OF CHEMISTRY

www.rsc.org/pccp

Surface Electrochemistry of CO_2 Reduction and CO Oxidation on Sm-doped CeO_{2-x}: Coupling between Ce^{3+} and Carbonate Adsorbates

Zhuoluo A. Feng[1, 2], Michael L. Machala[3], William C. Chueh[2, 3, *]

[1]Department of Applied Physics, Stanford University, Stanford, CA 94305

[2]Stanford Institute for Materials and Energy Sciences, SLAC National Accelerator Laboratory, Menlo Park, CA 94025

[3]Department of Materials Science and Engineering, Stanford University, Stanford, CA 94305

*To whom correspondence should be addressed: wchueh@stanford.edu

Abstract

The efficient electro-reduction of CO_2 to chemical fuels and the electro-oxidation of hydrocarbons for generating electricity are critical toward a carbon-neutral energy cycle. The simplest reactions involving carbon species in solid-oxide fuel cells and electrolyzer cells are CO oxidation and CO_2 reduction, respectively. In catalyzing these reactions, doped ceria exhibits mixed valence of Ce^{3+} and Ce^{4+}, and has been employed as a highly active and coking-resistant electrode. Here we report an in-operando investigation of the surface reaction mechanism on a ceria-based electrochemical cell using ambient pressure X-ray photoelectron spectroscopy. We show that the reaction proceeds via a stable carbonate intermediate, the coverage of which is coupled to the surface Ce^{3+} concentration. Under CO oxidation polarizations, both the carbonate and surface Ce^{3+}

concentration decrease with overpotential. Under CO_2 reduction polarizations, on the other hand, the carbonate coverage saturates whereas the surface Ce^{3+} concentration increases with overpotential. The evolution of these reaction intermediates was analyzed using a simplified two-electron reaction scheme. We propose that the strong adsorbate-adsorbate interaction explains the coverage-dependent reaction mechanism. These new insights into the surface electrochemistry of ceria shed light on the optimization strategies for better fuel cell electrocatalysts.

Key Words

Ceria, Carbonate, Adsorbate Coverage, Ambient Pressure XPS, Solid Oxide Fuel Cell

Introduction

Chemical and electrochemical reduction of CO_2 to useful gaseous and liquid fuels have attracted enormous attention[1-3]. The reverse reaction, the oxidation of CO, is also a crucial step in the catalytic conversion of automobile exhaust[4] and the oxidation of hydrocarbons for solid-oxide fuel cells[5-10]. The inherently stable carbon-oxygen bond in CO_2 and CO makes these reactions particularly challenging to catalyze at room temperature[11, 12]. Elevated-temperature solid-oxide fuel cells and electrolyzers, on the other hand, exhibit faster kinetics[13, 14]. The electrochemical reduction of CO_2 is expressed in Kröger-Vink notation as:

$$CO_{2\,(g)} + V_O^{\bullet\bullet} + 2e' \rightleftharpoons CO_{(g)} + O_O^{x} \quad (1)$$

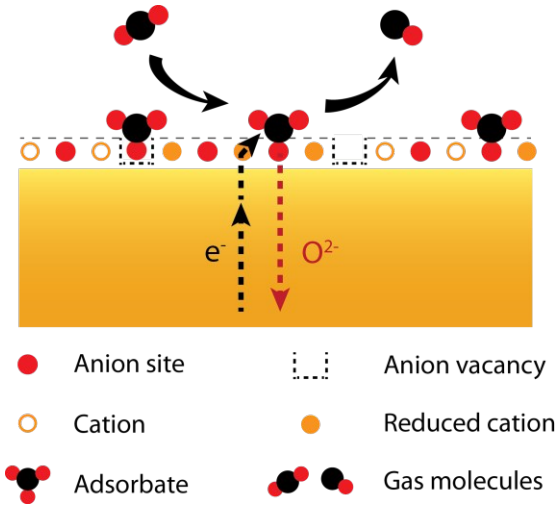

Fig. 1 Schematic of the oxygen-ion incorporation pathway on the surface of a mixed-ion-electron-conducting electrode.

where $V_O^{\cdot\cdot}$ denotes an oxygen vacancy, and $O_O^{\times}$ denotes a lattice oxygen. Here, the oxygen-ion-conducting electrolyte and electrode act as the oxygen sink (in the case of CO_2 dissociation) or the oxygen source (in the case of CO oxidation). The two-way traffic of the oxygen vacancies and electrons across the ceria/gas interface during oxygen incorporation reactions (Fig. 1), contrasts with the electron-transfer reactions in a typical metal/electrolyte junction in the solution-based electrocatalysis[15, 16]. This type of reaction underlies an increasing number of chemical conversion and energy storage devices. Encouraging results have been reported at temperatures between 600 ˚C and 800 ˚C in the case of CO_2 electrolysis[17, 18]. Similar success was also reported in the solar-driven, thermochemical dissociation of CO_2 to CO using oxygen-storing metal oxides[19, 20]. Heating the metal oxides with concentrated sunlight reduces the solid and generates oxygen vacancies. Subsequently, the oxygen-deficient oxides are re-oxidized by CO_2 at a lower temperature, producing CO, a key precursor towards liquid fuel synthesis.

Promising efficiencies at essentially complete selectivity towards CO have been demonstrated[21].

In both elevated-temperature electrochemical and thermochemical reduction of CO_2 and oxidation of CO, oxygen-deficient CeO_2 (ceria) is one of the most commonly employed materials, owing to the relative ease at which oxygen vacancies form upon decreasing oxygen pressure, increasing temperature, and aliovalent doping[22]. In an electrochemical cell, the electrochemically-generated oxygen vacancies and Ce^{3+} react with gaseous CO and CO_2 species. The general reaction shown in Equation 1 can be written specifically for ceria as:

$$CO_{2\,(g)} + V_O^{\bullet\bullet} + 2Ce_{Ce}^{'} \rightleftharpoons CO_{(g)} + O_O^{\times} + 2Ce_{Ce}^{\times} \qquad (2)$$

where $Ce_{Ce}^{'}$ represents the Ce^{3+} cations, or localized electrons, and $Ce_{Ce}^{\times}$ represents the Ce^{4+} cations. Additionally, ceria's low catalytic activity towards carbon deposition eliminates the possibility of coking on the surface, even under thermodynamically favorable conditions[7, 8, 21].

The non-electrochemical oxidation of CO and reduction of CO_2 on ceria have been examined extensively for the past few decades. The majority of the work has been focused on identifying the adsorbate species under either a CO or a CO_2 atmosphere[23-28]. It is generally agreed that in a CO_2 atmosphere, the surface of ceria is covered mainly with carbonate species. Furthermore, density functional theory calculations have shown that it is energetically favored for the CO_2 activation and the CO oxidation to take place near surface oxygen vacancies[29-31]. This has also been shown for H_2O splitting, both computationally[32-35] and experimentally[36]. Traditionally, these catalytic reactions

involving CO and CO_2 have been catalyzed by metal supported on ceria via a spillover pathway[37-39]. Recently, however, there has been growing evidence showing the importance of reactions catalyzed purely by ceria[40-45].

On the other hand, electrochemical redox processes, unlike chemical processes, are typically carried out in an atmosphere containing a mixture of CO and CO_2[46, 47]. The reducing atmosphere of the gas mixture leads to a partial reduction of ceria to the Ce^{3+} state[24, 48]. Adding additional complexity, the electrochemical polarization can further modulate the degree of reduction of the bulk and surface of ceria, which is expected to have a significant effect on the reaction pathway. The mechanism of these electrochemical reactions have been explored primarily using current-voltage polarization and impedance spectroscopy, though the precise identification of the reaction pathway has been challenging[46, 47, 49, 50]. Recently, electrochemical measurements and X-ray spectroscopies have been combined to investigate ceria electrodes in elevated-temperature solid-state cells[44, 51-53], as well as in room-temperature liquid cells[54, 55]. In particular, Yu *et al.* have explored the spatial distribution of electrochemical reactions involving CO and CO_2 using in-situ photoelectron spectroscopy, where they observed the reduction of CO_2 to graphitic carbon under relatively large overpotentials[56], as previously observed via Raman spectroscopy in hydrocarbon fuel[57, 58]. Because a diffusion-limited cell was employed, quantitative analysis of the reaction pathway was difficult.

In this work, we employ ambient pressure X-ray photoelectron spectroscopy (APXPS) to investigate the mechanism of the electrochemical dissociation of CO_2 and oxidation of CO on a water-free surface of Sm-doped CeO_2 (SDC) thin-film electrodes under realistic reaction conditions. Doping ceria with trivalent samarium generates

oxygen vacancies, and yields high oxygen ion conductivity under both oxidizing and reducing conditions. We show that both the electrochemical reduction and oxidation reactions proceed via a stable CO_3^{2-} intermediate, consistent with previous work[49]. Under electrochemical CO oxidation (anodic) conditions, the carbonate coverage varies linearly with the surface Ce^{3+} concentration, suggesting a rapid quasi-equilibrium between the two species. On the other hand, with increasing CO_2 reduction (cathodic) overpotential, the surface is quickly saturated with CO_3^{2-}. Our direct observation suggests that the height of the energetic barrier in the rate-determining step during CO_2 dissociation is possibly modified under high carbonate coverage conditions due to strong adsorbate-adsorbate interactions.

Experimental and Theoretical Methods

Sample preparation. The single-environment, solid-state electrochemical cell was fabricated on a 10×10×0.5 mm $Y_{0.16}Zr_{0.84}O_{1.92}$ (YSZ) (100) single crystal substrate (MTI Corp.), which also served as the solid electrolyte (Fig. 2a). The working electrode (WE) consists of a 450 nm thick $Sm_{0.2}Ce_{0.8}O_{1.9-x}$ dense thin film grown by pulsed-laser deposition (PLD). Buried, micro-patterned Pt stripes served as the current collector, which eliminates the lateral variation in the electrochemical current density and simplifies the interpretation compared with previous work[52, 56]. The counter electrode (CE) consists of 80 nm thick porous Pt sputtered on a 50 nm thick SDC interlayer, also grown by PLD. Details of the fabrication process and physical characterization have been reported previously[53].

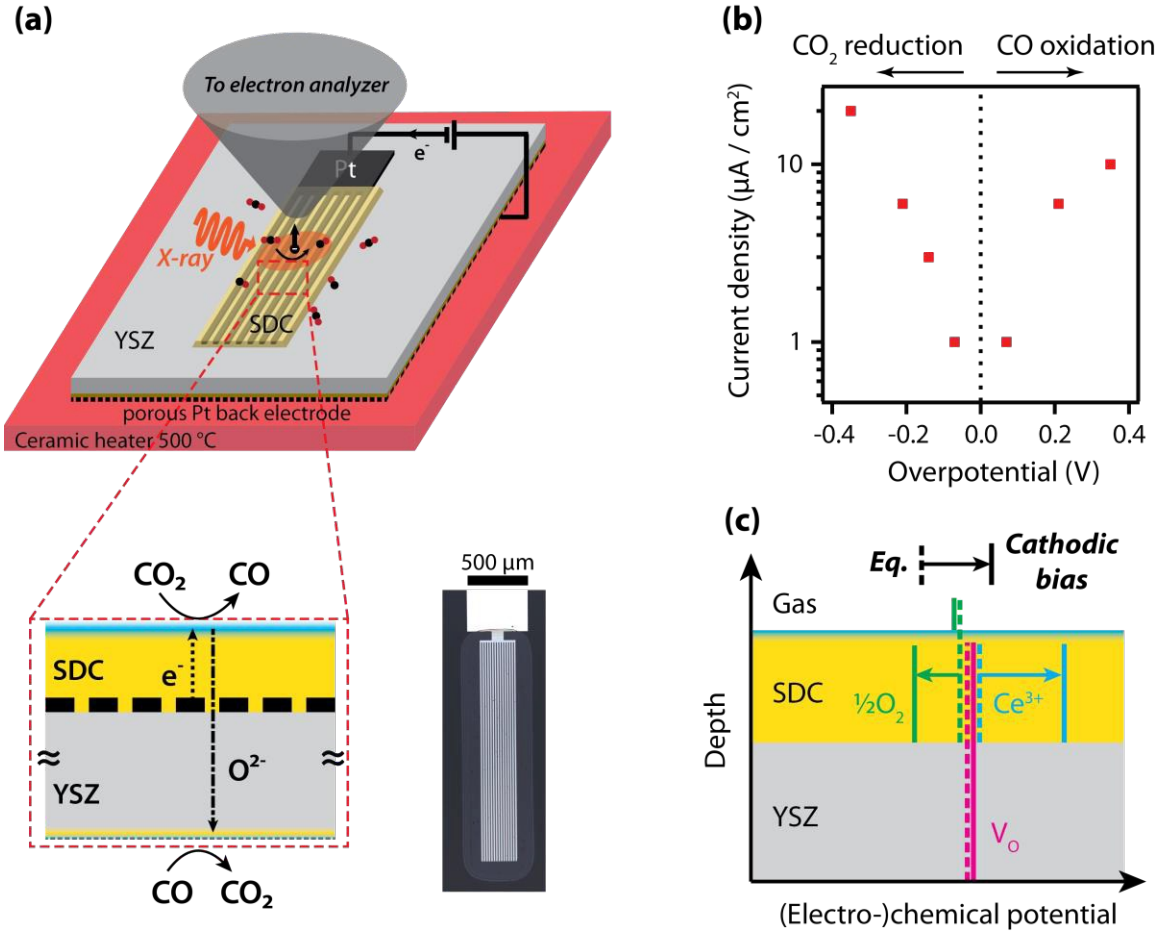

Fig. 2 Overview of the experimental setup. (a) A schematic depicting the sample geometry, a cross-sectional view of the reaction pathway, and an optical micrograph of the ceria electrode. (b) Current-voltage characteristics of the cell at 500 ˚C in 270 mTorr CO/CO_2 mixture. (c) The change of (electro-) chemical potential of effective oxygen gas (green), oxygen vacancies (magenta) and Ce^{3+} (cyan) from the equilibrium state (dashed lines) to the cathodically biased state (solid lines).

Electrochemical APXPS. Operando X-ray photoelectron spectroscopy was carried out by APXPS at the beam line 9.3.2 of the Advanced Light Source (Lawrence Berkeley National Laboratory), which is equipped with a differentially pumped Scienta R4000 HiPP electron analyzer. The electrochemical cell was preconditioned at 500 ˚C in 5×10^{-5} Torr O_2 before 250 mTorr CO_2 and 20 mTorr CO was introduced into the vacuum

chamber (Fig. 2). An electrical bias was applied between the WE and CE using a Bio-Logic SP-300 potentiostat. The current-voltage curve is shown in Fig. 2b. Overpotential at the WE was quantified via the rigid shift of the Ce $4d_{3/2}$ photoelectron peak[53, 59] (see Fig. S1). The binding energy of all photoemission spectra are first calibrated to the Au $4f_{7/2}$ peak (83.8 eV), and then shifted such that the Ce 4d X''' peak at different overpotentials are aligned at its open-circuit value[27].

Non-equilibrium defect chemistry. We briefly describe the (electro-)chemical potential distribution within the single-environment electrochemical cell at open circuit and under bias. At open-circuit condition, both the WE and CE are equilibrated with the oxygen partial pressure, $p_{O_2}^{eq}$, and the uniform gas environment gives a zero voltage across the cell (superscript 'eq' denotes equilibrium). When an electrical bias is applied between the electrodes (specifically between the two metal film current collectors), the local partial pressure of oxygen at the two electrodes deviate from equilibrium values (well-defined at the Pt/YSZ/SDC junction at the WE and at Pt/SDC/gas junction at the CE). The polarization drives symmetric, electrolysis half-reactions (forward and reverse of Equation 2). For the purpose of this theoretical analysis, we assume that the overpotential at the CE and the electrolyte is negligible, electron transfer between Pt and SDC is fast compared to the rate-limiting step, and bulk transport within SDC is fast. Combined, these assumptions imply that the overpotential occurs at the SDC/gas interface. As a result, under bias, the oxygen partial pressure at the CE remains equilibrated with $p_{O_2}^{eq}$ and the electrostatic potential within the YSZ remains unchanged. Thus, the effective oxygen partial pressure in the bulk of the WE, $p_{O_2}^{WE}$, is uniform and can be determined by the Nernst equation:

$$\eta = \frac{k_B T}{4e} \ln\left(\frac{p_{O_2}^{WE}}{p_{O_2}^{eq}} \right) \quad (3)$$

where η is the applied overpotential, k_B is the Boltzmann constant, T is the temperature and e is the elementary charge. Invoking the local equilibrium approximation within the bulk of the SDC WE, we write the following equilibrium condition using the SDC defect chemistry in Equation 2 (as well as the equilibrium between $O_{2(g)}$, $CO_{(g)}$ and $CO_{2(g)}$):

$$\Delta\tilde{\mu}_{V_O^{\bullet\bullet}} + 2\Delta\tilde{\mu}_{Ce_{Ce}^{'}} + \frac{1}{2} k_B T \ln\left(\frac{p_{O_2}^{WE}}{p_{O_2}^{eq}} \right) = 0 \quad (4)$$

where Δ denotes the difference between equilibrium and off-equilibrium (i.e., biasing), and $\tilde{\mu}$ is the electrochemical potential. Combining Equation 3 and 4, we obtain

$$e\eta = -\frac{1}{2}\Delta\tilde{\mu}_{V_O^{\bullet\bullet}} - \Delta\tilde{\mu}_{Ce_{Ce}^{'}} = -\frac{1}{2}\Delta\mu_{V_O^{\bullet\bullet}} - \Delta\mu_{Ce_{Ce}^{'}} \quad (5)$$

We cancel out the electrostatic potential terms contained in the electrochemical potential, leaving only the chemical potential μ. In heavily-doped SDC, the chemical potential of oxygen vacancies can be approximated as constant under bias. Therefore, we have

$$e\eta \approx -\Delta\mu_{Ce_{Ce}^{'}} \quad (6)$$

which is also illustrated schematically in (Fig. 2c). Finally, in the limit of dilute defect concentration, we relate the electron concentration in the SDC WE to the overpotential:

$$c_{Ce_{Ce}^{'}} \approx c_{Ce_{Ce}^{'}}^{eq} \exp\left(-\frac{e\eta}{k_B T} \right) \quad (7)$$

This relationship illustrates that the electrical bias directly controls the redox-state of SDC via non-equilibrium thermodynamics when the SDC/gas interfacial reaction is

rate-limiting. Subsequently, the variation in electron concentration drives (electro-)chemical reaction at the gas/solid interface.

Results

We carried out electrochemical CO oxidation and CO_2 reduction using a microfabricated solid-state electrochemical cell in a mixture of 250 mTorr CO_2 and 20 mTorr CO gas at 500 ˚C, the ratio of the two being similar to that employed in a typical solid-oxide electrolyzer (Fig. 2). Under CO_2 electro-reduction conditions (Fig. 2a), the electrons from the current collector migrate to the surface and reduce CO_2, while at the same time the oxygen vacancies migrate from the counter electrode to the surface. The reverse reaction takes place during CO electro-oxidation. We tracked the evolution of the photoemission spectra with the overpotential between −0.35 V and 0.35 V (negative values corresponding to electro-reduction). To eliminate complexity due to hysteresis, spectroscopy measurements were made after the current stabilized at each potential. See Fig. S2(a) for the time-dependent voltage and current curves. We further confirmed that the electrode had reached steady-state by verifying that the spectra did not change at the beginning and end of the spectroscopy measurement for a given overpotential (Fig. S2(b)).

Fig. 3 shows the normalized O 1s and C 1s photoemission spectra during both CO_2 electro-reduction and CO electro-oxidation at an information depth of ~0.6 nm. In the O 1s spectra (Fig. 3a), three peaks have been fitted by constraining equal full-width-half-maximum. The primary peak in blue (~529.1 eV) is assigned to the lattice oxygen of Sm-doped ceria, consistent with previous observations[53]. The minor peak in grey at

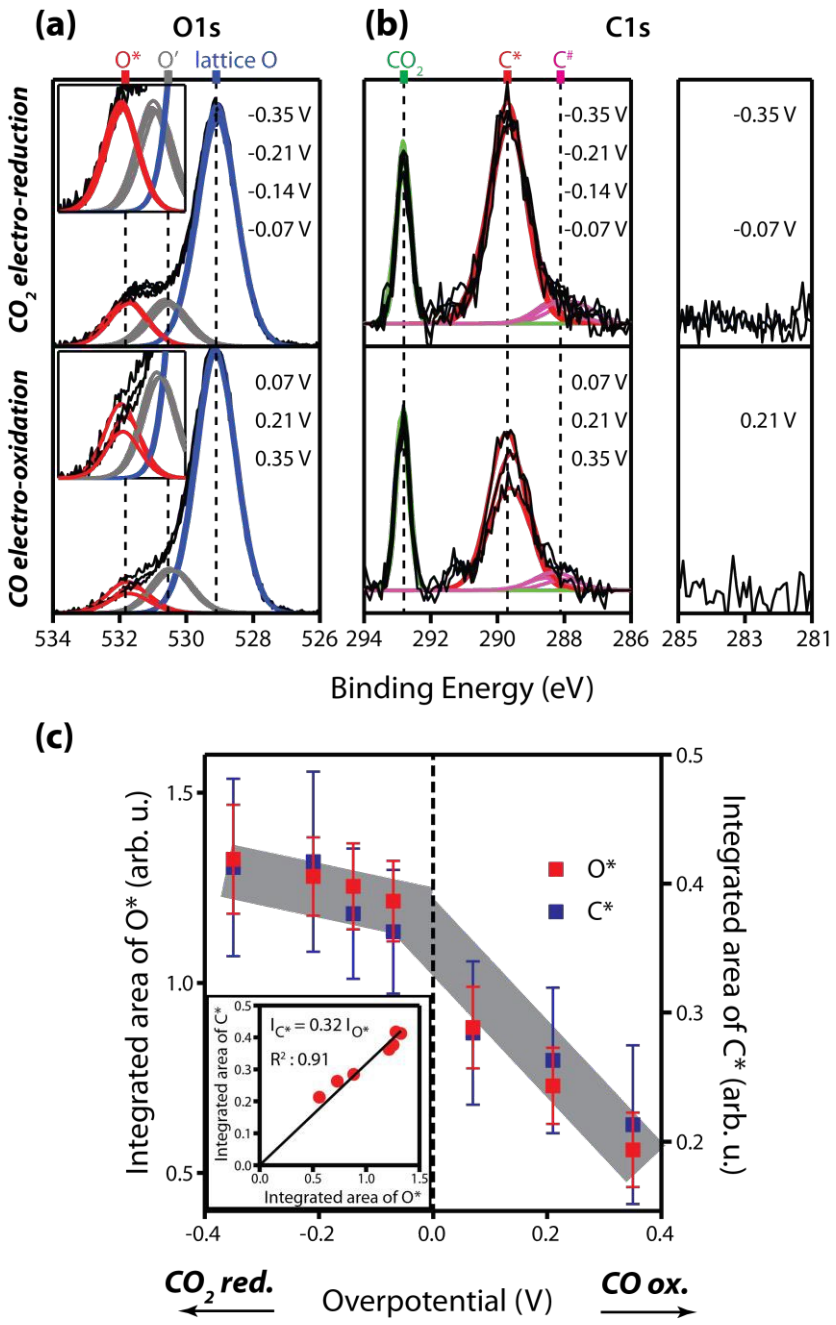

Fig. 3 The response of carbonate reaction intermediate to the electrochemical polarization in 250 mTorr CO_2 and 20 mTorr CO at 500 ˚C. (a) O 1s spectra under CO_2 electro-reduction (top) and CO electro-oxidation (bottom) conditions; (b) C 1s spectra under CO_2 electro-reduction (top) and CO electro-oxidation (bottom) conditions. (c) Integrated peak areas of C* and O* as a function of the overpotential. The inset shows the linear relationship between the integrated area of C* and O* under polarization. The O 1s and C 1s spectra were taken at a photon energy of 690 eV and 490 eV, respectively. The information depth of XPS is about 0.6 nm. The intensities of the O 1s spectra were normalized to the same background intensity (averaged between 524 and 526 eV) while

those of the C 1s spectra were normalized by the gas phase CO_2 peak. Binding energy calibration method is described in the experimental section.

~1.4 eV to the left of the lattice O peak (denoted as O') is attributed to Si impurity[53]. The photoemission feature in red (denoted as O*) with a binding energy ~2.6 eV greater than that of the lattice O disappears when the chamber is pumped out to high vacuum at 500 ˚C (see Fig. S3), and therefore must be due to the surface adsorbates from the gas phase. Compared with previously reported values, the binding energy of this red peak relative to the lattice O suggests that it corresponds to carbonate-related adsorbates[37, 60]. Lastly, we did not observe peaks corresponding to adsorbed OH (with binding energy ~2.2 eV relative to the lattice oxygen), as expected for the hydrogen and water-free environment of our experiment. The silicon impurity peak remains invariant with overpotential (Fig. 3a).

Turning to the C1s spectra (Fig. 3b), a total of three peaks were observed. The pronounced peak in green is attributed to the gas-phase CO_2, consistent with the peak assignment in the literature[61]. The remaining C1s peaks are assigned to carbon-containing adsorbates because of their disappearance under high vacuum conditions at 500 ˚C (Fig. S3). It is generally agreed that the peak in red at ~289.7 eV (labeled as "C*" in Fig. 3a), originates from adsorbed carbonate species[37, 56, 60], although the precise molecular structure is still under debate[26, 27]. Plotting the integrated area of C* peak against that of the O* peak gives a straight line through the origin (Fig. 3c, inset). This confirms that they arise from the same carbonate adsorbate. The adsorbate's binding energy is known to depend on the oxidation state of the ceria surface, as shown by

Albrecht *et al.*[27] Whereas we calibrated our binding energies to a gold foil, Albrecht *et al*. calibrated the binding energies relative to the Ce 4d X''' peak. This resulted in a 1 eV difference in the observed binding energies between the two experiments. We accounted for this difference and compared the C1s binding energy of the carbonate adsorbate. The adjusted binding energy is 290.7 eV. Based on the report by Albrecht *et al*., this value suggests that the carbonate adsorbed in the vicinity of Ce^{3+} cations. We note, however, that the O1s binding energy of the carbonate adsorbate does not agree with that reported by Albrecht. This could be attributed to the presence of Sm dopant in our electrode.

The assignment of the minority peak at ~288.1 eV (labeled it as "$C^{\#}$"), however, is less definitive. Some researchers have assigned it to carboxylate species (a CO^{2-} adsorbed atop a Ce cation) based on infrared reflection absorption spectroscopy and X-ray photoelectron spectroscopy measurements[23, 37]. Others have argued that carboxylate is unstable on the surface of ceria and assigned it to other forms of carbonate species[26]. Because this peak remains a minor component of the C1s spectra under all conditions examined, we do not consider it further.

Fig. 3c shows the quantified O* and C* peak area as a function of applied overpotential. Interestingly, these peaks exhibit a non-linear dependence. Under CO electro-oxidation conditions, the carbonate peak decreases with increasing anodic overpotential. In contrast, under CO_2 electro-reduction conditions, the intensity of the carbonate peaks remains essentially constant with cathodic overpotential.

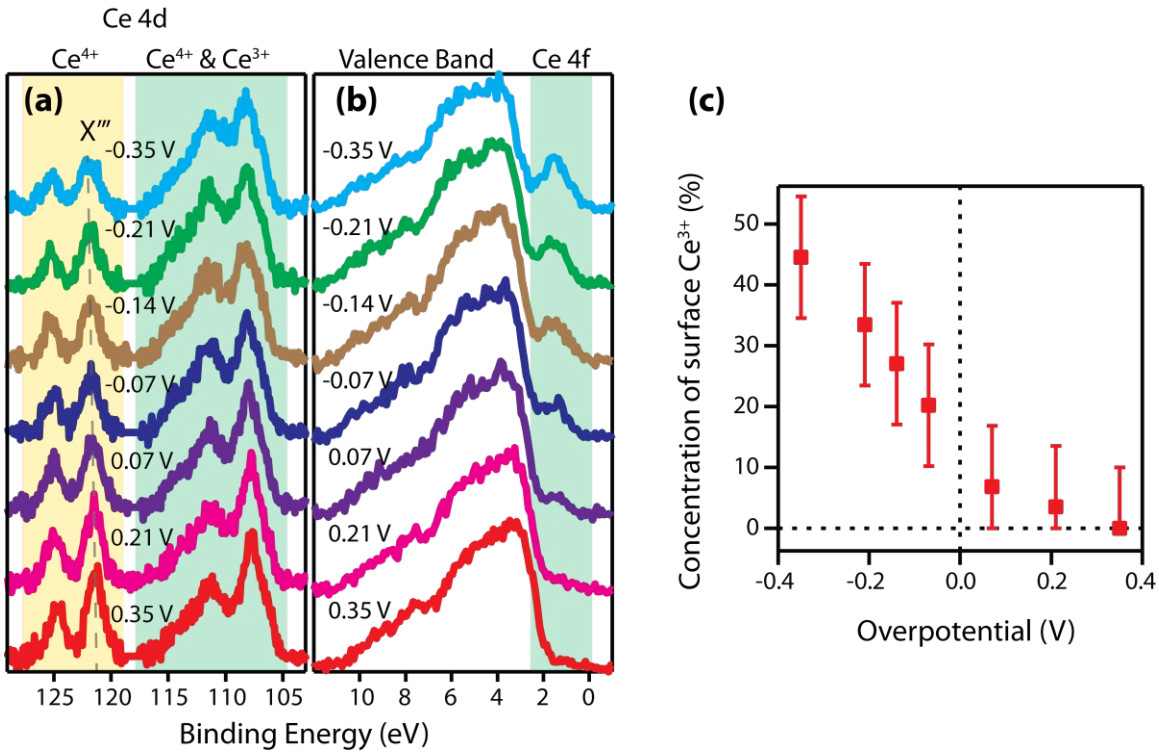

Fig. 4 The response of Ce oxidation state to the electrochemical polarization. (a) Ce 4d core-level spectra. The peaks highlighted in yellow are due to the Ce^{4+} oxidation state, whereas the peaks highlighted in green are due to both Ce^{3+} and Ce^{4+} states. (b) Valence-band spectra. The peak at a binding energy of ~ 1.5 eV corresponds to the Ce 4f electronic state occupied by the Ce^{3+} localized electrons. (c) The quantified Ce^{3+} concentration as a function of overpotential. The Ce 4d and valence band spectra were taken at photon energy of 370 eV and 250 eV, respectively. The information depth is about 0.6 nm. The intensity of the spectra is normalized by the total intensity arising from all Ce cations. Therefore, the intensity of the Ce 4f state in the valence band spectra directly corresponds to the Ce^{3+} concentration. The error bars in (c) are due to the finite resolution of the XPS electron analyzer and truncated at 0% to be physically meaningful.

In addition to the adsorbed carbonate species, the localized electrons resulting from the reduction of Ce^{4+} to Ce^{3+} also play a critical role in the surface reactions[62, 63]. The photoemission signature of the Ce^{3+} localized electrons is well characterized by the present and other authors[51, 53, 64]. To briefly summarize, final state effects in the Ce 4d photoelectron spectrum lead to the splitting of the peaks, with the two highest binding energy components arising purely from the Ce^{4+} state; in the valence band spectra, the

peak at ~ 1.5 eV binding energy corresponds to the occupied Ce 4f electronic state, which directly represents the Ce^{3+} oxidation state. Fig. 4 shows the systematic variation of both Ce 4d and the valence-band spectra with the overpotential, measured at an information depth of ~ 0.6 nm. Even in the absence of quantitative analysis, the valence band spectra (Fig. 4b) clearly shows that the occupied Ce 4f states decreases upon CO oxidation and increases upon CO_2 reduction, consistent with the expected bulk behavior (Equation 7). Using a previously validated quantification procedure (Fig. S4)[64], we determined the concentration of Ce^{3+} on the surface from the Ce 4d and the Ce 4f (valence band) photoemission spectra (Fig. 4c). Under the most anodic overpotential of 0.35 V, the surface Ce is essentially fully oxidized in the 4+ oxidation state, while at the most cathodic overpotential −0.35 V, the surface is enriched with 45% of Ce^{3+}, meaning that almost half of the Ce cations in the near-surface region are in the 3+ oxidation state. As shown earlier, under cathodic overpotentials, the equilibration of the Fermi level in the metal current collector and the ceria working electrode directly results in an increase in the chemical potential of electrons (i.e., of Ce^{3+}), and vice versa upon anodic overpotential (Fig. 2c). We have recently demonstrated that the strong coupling between the Ce^{3+} and the overpotential is due to the fast transport of localized electrons between the surface and the bulk[53]. We note that the surface electron concentration is higher than that predicted by the bulk thermodynamics due to defect segregation (i.e., lower formation energy at the surface than in the bulk).

As can be seen in Fig. 3 and 4, the carbonates and the Ce^{3+} localized electrons exhibit different scaling with overpotential. We plot the intensity of the carbonate peak versus the Ce^{3+} concentration at various overpotentials (Fig. 5a). Two distinctive regimes

are revealed. Under anodic overpotentials (CO electro-oxidation), the coverage of carbonate is low and increases sharply and linearly with the Ce^{3+} concentration. Under cathodic overpotentials (CO_2 electro-reduction), in contrast, the carbonate coverage remains relatively constant while the Ce^{3+} concentration increases. The asymmetric behavior suggests a reaction pathway that is coverage-dependent.

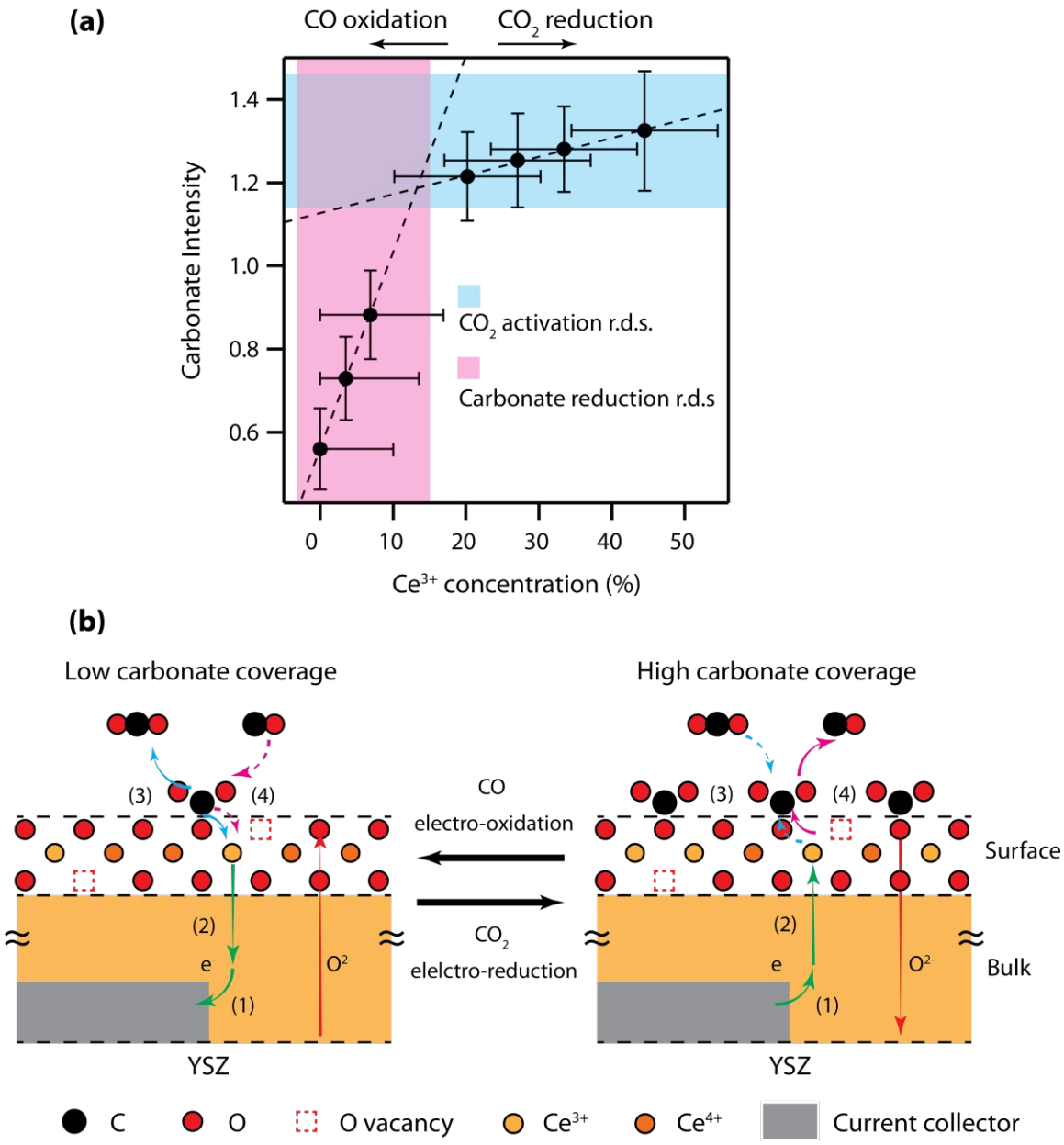

Fig. 5 Proposed reaction mechanism. (a) The correlation between the carbonate coverage and the concentration of surface Ce^{3+} localized electrons. (b) The reaction pathway divided schematically into four steps. In the CO_2 electro-reduction direction (on the right), step (1) and (2) are the electron transfer from the Pt current collectors to the surface Ce cations, depicted in green. Step (3) is the CO_2 adsorption and the first electron transfer. Step (4) is the second electron transfer and oxygen ion incorporation resulting in decomposition of carbonate into CO. The dotted lines represent the rate-determining steps.

Discussion

To understand the correlation between the Ce^{3+} concentration and the carbonate coverage, we propose a simplified reaction pathway (Fig. 5b). The global reaction Equation (2) consists of a sequence of bulk and surface processes (written in the CO_2 electro-reduction direction):

Step 1
$$\begin{cases} 2\left(Ce^{\times}_{Ce,\,b} + e^{-}_{M} \rightleftharpoons Ce^{'}_{Ce,\,b}\right) \\ V^{\cdot\cdot}_{O,\,YSZ} \rightleftharpoons V^{\cdot\cdot}_{O,\,b} \end{cases} \quad (8)$$

Step 2
$$\begin{cases} 2\left(Ce^{'}_{Ce,\,b} \rightleftharpoons Ce^{'}_{Ce,\,s}\right) \\ V^{\cdot\cdot}_{O,\,b} \rightleftharpoons V^{\cdot\cdot}_{O,\,s} \end{cases} \quad (9)$$

Step 3
$$CO_{2\,(g)} + O^{\times}_{O,\,s} + Ce^{'}_{Ce,\,s} \rightleftharpoons \left(CO_3\right)^{'}_{O,\,s} + Ce^{\times}_{Ce,\,s} \quad (10)$$

Step 4
$$\left(CO_3\right)^{'}_{O,\,s} + Ce^{'}_{Ce,\,s} + V^{\cdot\cdot}_{O,\,s} \rightleftharpoons CO_{(g)} + 2O^{\times}_{O,\,s} + Ce^{\times}_{Ce,\,s} \quad (11)$$

where the subscripts ‘b’, ‘s’, ‘M’ and ‘YSZ’ denote the bulk and surface species of the ceria electrode, the metal current collector, and the YSZ electrolyte, respectively. We note that these reactions are unlikely the true elementary steps. In the CO_2 electro-reduction direction, the reaction begins with the electron transfer from the current

collector to the bulk of the ceria electrode, and the oxygen vacancy transfer from the solid electrolyte to the ceria electrode (step 1). Next, these mobile species migrate to the surface (step 2). We then divide the surface reaction conceptually into two single-electron transfer steps. In step 3, a physisorbed CO_2 molecule (likely a linear structure) is activated by the localized electron (Ce^{3+}) from the ceria electrode, generating a carbonate adsorbate $\left(CO_3\right)'_{O,s}$ (likely bent). This step is then followed by a second electron transfer and the ion incorporation reaction, which decomposes the carbonate and generates an adsorbed CO, which finally desorbs from the surface (step 4)[65]. Step 1 and 2, the solid-solid charge-transfer reactions, are not rate-determining, as shown recently by Chueh *et al*. on the basis of electrochemical impedance spectroscopy[40], and more recently by Feng *et al.* using photoemission spectroscopy[53]. Therein, it was also shown that the bulk and near-surface migration of localized electrons and oxygen vacancies are not rate-determining. Thus, the rate-determining steps are those occurring at the ceria-gas interface (step 3 and 4).

Electron transfer between Ce^{3+} and the carbonate is crucial for the activation and reduction of CO_2 molecule and likewise the oxidation of CO. Two electrons are transferred between ceria and the carbonate adsorbate. This contrasts with one electron transferred per hydroxyl adsorbate in the case of H_2O dissociation and H_2 oxidation. The correlation between surface Ce^{3+} concentration and carbonate coverage, determined experimentally in this work, reflects the relative rate constants of the reaction steps proposed above. Under CO electro-oxidation conditions, we observed that the carbonate coverage exhibits a strong and linear-like relationship to the surface Ce^{3+} concentration. We propose that the behavior arises from the high rate constant of the electron transfer in

step 3 relative to other steps. In other words, the reactant and products (Ce^{3+}, carbonate adsorbate, etc.) are quasi-equilibrated. As a direct result, the surface carbonate coverage is tuned electrochemically by the overpotential. Because the surface Ce^{3+} concentration decreases with anodic overpotential due to the oxidation of ceria (Fig. 2c), the quasi-equilibrium leads to the decreasing carbonate coverage with increasing anodic overpotential.

Based on the observation that electron transfer in step 3 is fast, we speculate the ion/electron transfer reaction in step 4 is likely rate-determining. Our proposal contrasts with the work by Yu *et al.*, which attributed the correlation between Ce^{3+} and carbonate to slow reaction kinetics. As discussed here and in an earlier work[53], in oxide electrodes with variable stoichiometry, such as ceria, the change in the concentration of reaction intermediates does not necessarily indicate that they are participating in the rate-determining step.

Next we turn to CO_2 electro-reduction, under which the surface Ce^{3+} concentration increases due to the electro-reduction of the electrode (Fig. 4). Unlike CO electro-oxidation, the carbonate coverage does not vary significantly with the surface Ce^{3+} concentration (Fig. 5). At the same time, the carbonate coverage is consistently higher than that under CO electro-oxidation conditions. This saturation of the carbonate adsorbates takes place at a cathodic overpotential of ~ 0.1 V. The precise coverage is difficult to quantify due to the lack of a standard, but is approximately 20 % (neglecting attenuation effects). We attribute the switchover of the correlation shown in Fig. 5 to the carbonate coverage effect. As the coverage increases, adsorbate-adsorbate interaction is expected to increase, especially given the relatively large molecular dimension of the

carbonate species, compared to adsorbates such as hydroxyl and atomic oxygen. This saturation behavior was not observed in a similar experiment under H_2/H_2O atmosphere, despite the hydroxyl coverage being similar to the adsorbate coverage observed here[53]. Indeed, a recent density functional calculation reported that the carbonate adsorption enthalpy depends strongly on its coverage of the CeO_2 (111) surface[66]. The authors showed that as the coverage of surface carbonate increases to about 1/3, the adsorption enthalpy begins rising dramatically, making CO_2 adsorption more difficult. Our experimental observation of the saturation under CO_2 dissociation condition lends support to this theory.

The saturation of carbonate intermediate under increasingly cathodic overpotential has direct implication on the kinetics of the CO_2 reduction reaction. In step 3 of the simplified reaction pathway, an electron is transferred from the surface to the adsorbed CO_2. As carbonate-carbonate interaction increases, the chemical potential of the adsorbate increases at a given coverage. In turn, this lowers the driving force of the reaction step. Specifically, while the electrochemical potential of the Ce^{3+} (Fermi level) increases and drives the step 3 in the forward direction, the increase in the chemical potential of the carbonate (a product species) opposes this change. In other words, the surface of ceria is less capable of supplying electrons to the CO_2 molecules. While we do not have direct experimental evidence, we speculate that at a critically high coverage, step 3, rather than step 4, could become rate-determining at sufficiently large cathodic overpotentials.

Conclusion

Using operando APXPS, we tracked the evolution of the stable carbonate reaction intermediate and surface Ce^{3+} localized electrons under CO electro-oxidation and CO_2 electro-reduction conditions on doped ceria surface. Two electrons are transferred per carbonate formation during the electrochemical reaction, and the relative rates of these electron-transfer processes determine the reaction pathway. Under CO oxidation polarization, the surface becomes more oxidized, and the carbonate coverage vanishes. This observation suggests that the electron transfer between ceria and the adsorbed carbonate is likely rate limiting. Under CO_2 reduction polarization, on the other hand, the surface becomes more reduced. At the same time, the carbonate coverage saturates. This is likely due to strong adsorbate-adsorbate interaction, which in turn lowers the driving force for the reduction of CO_2 to carbonate. This observation contrasts with measurements under H_2/H_2O gas mixture, where comparably smaller molecular size of the OH intermediate relative to the carbonate intermediate do not give rise to adsorbate-adsorbate interaction. In a practical solid-oxide electrochemical cell, the partial pressure of CO/CO_2 is two to three orders magnitude higher than that employed in this work, meaning the adsorbate coverage and adsorbate-adsorbate interaction is likely larger than that observed here, and plays an even more significant role in determining the reaction pathway.

Acknowledgement

The authors would like to acknowledge the School of Engineering and the Precourt Institute for Energy at Stanford University for the start-up funding of this work. Z. A. F. was supported by the Gordon and Betty Moore Foundation through Grant GBMF2573 to Z.-X. Shen and by the National Science Foundation under Award #1336835. M. L. M. was supported by the National Science Foundation Graduate Research Fellowship under Grant No. DGE-114747. The Advanced Light Source is supported by the Director, Office of Science, and Office of Basic Energy Sciences, of the U.S. Department of Energy under Contract No. DE-AC02-05CH11231. We thank Z. Liu, R. Chang, B. Mao and S. Axnanda for their experimental assistance at the Advanced Light Source. Lastly, we are grateful for the insightful discussion with Prof. Z.-X. Shen.

Author Contribution

Z. A. F. and W. C. C. conceived the experiment. Z. A. F. prepared the samples. Z. A. F. and M. L. M. performed the spectroscopy measurement. Z. A. F. analyzed the data. All authors contributed to writing the manuscript. W. C. C. supervised the project.

Supporting Information

Supplementary Fig. S1-S4.

Notes

The authors declare no competing financial interest.

References

1. V. Havran, M. P. Dudukovic and C. S. Lo, *Ind. Eng. Chem. Res.*, 2011, **50**, 7089-7100.
2. G. Centi and S. Perathoner, *Catal. Today*, 2009, **148**, 191-205.
3. Y. Yan, E. L. Zeitler, J. Gu, Y. Hu and A. B. Bocarsly, *J. Am. Chem. Soc.*, 2013, **135**, 14020-14023.
4. J. Kaspar, P. Fornasiero and N. Hickey, *Catal. Today*, 2003, **77**, 419-449.
5. A. Atkinson, S. Barnett, R. J. Gorte, J. T. S. Irvine, A. J. Mcevoy, M. Mogensen, S. C. Singhal and J. Vohs, *Nat. Mater.*, 2004, **3**, 17-27.
6. T. Hibino, A. Hashimoto, T. Inoue, J. Tokuno, S. Yoshida and M. Sano, *Science*, 2000, **288**, 2031-2033.
7. E. P. Murray, T. Tsai and S. A. Barnett, *Nature*, 1999, **400**, 649-651.
8. S. D. Park, J. M. Vohs and R. J. Gorte, *Nature*, 2000, **404**, 265-267.
9. S. Ahmed and M. Krumpelt, *Int. J. Hydrogen Energ.*, 2001, **26**, 291-301.
10. F. Joensen and J. R. Rostrup-Nielsen, *J. Power Sources*, 2002, **105**, 195-201.
11. H. J. Freund and M. W. Roberts, *Surf. Sci. Rep.*, 1996, **25**, 225-273.
12. Y. Toda, H. Hirayama, N. Kuganathan, A. Torrisi, P. V. Sushko and H. Hosono, *Nat. Commun.*, 2013, **4**, 2378.
13. D. J. L. Brett, A. Atkinson, N. P. Brandon and S. J. Skinner, *Chem. Soc. Rev.*, 2008, **37**, 1568-1578.
14. W. C. Chueh and S. M. Haile, *Annu. Rev. Chem. Biomol.*, 2012, **3**, 313-341.
15. A. J. Bard and L. R. Faulkner, *Electrochemical methods: fundamentals and applications*, Wiley New York, 2001.
16. J. O. M. Bockris and A. K. N. Reddy, *Modern electrochemistry: fundamentals of electrodics*, Springer, 2000.
17. Z. Zhan, W. Kobsiriphat, J. R. Wilson, M. Pillai, I. Kim and S. A. Barnett, *Energ. Fuels*, 2009, **23**, 3089-3096.
18. Q. X. Fu, C. Mabilat, M. Zahid, A. Brisse and L. Gautier, *Energ. Environ. Sci.*, 2010, **3**, 1382-1397.
19. W. C. Chueh, C. Falter, M. Abbott, D. Scipio, P. Furler, S. M. Haile and A. Steinfeld, *Science*, 2010, **330**, 1797-1801.
20. P. Furler, J. R. Scheffe and A. Steinfeld, *Energ. Environ. Sci.*, 2012, **5**, 6098-6103.
21. W. C. Chueh and S. M. Haile, *ChemSusChem*, 2009, **2**, 735-739.
22. A. Trovarelli, *Catal. Rev. Sci. Eng.*, 1996, **38**, 439-520.

23. C. Li, Y. Sakata, T. Arai, K. Domen, K. Maruya and T. Onishi, *J. Chem. Soc. Farad. T. 1*, 1989, **85**, 929-943.
24. T. Jin, T. Okuhara, G. J. Mains and J. M. White, *J. Phys. Chem.*, 1987, **91**, 3310-3315.
25. T. Jin, Y. Zhou, G. J. Mains and J. M. White, *J. Phys. Chem.*, 1987, **91**, 5931-5937.
26. G. N. Vayssilov, M. Mihaylov, P. St Petkov, K. I. Hadjiivanov and K. M. Neyman, *J. Phys. Chem. C*, 2011, **115**, 23435-23454.
27. P. M. Albrecht, D.-e. Jiang and D. R. Mullins, *J. Phys. Chem. C*, 2014, **118**, 9042-9050.
28. C. Binet, M. Daturi and J. C. Lavalley, *Catal. Today*, 1999, **50**, 207-225.
29. Z. Cheng, B. J. Sherman and C. S. Lo, *J. Chem. Phys.*, 2013, **138**, 014702.
30. T. X. T. Sayle, S. C. Parker and C. R. A. Catlow, *Surf. Sci.*, 1994, **316**, 329-336.
31. T. X. T. Sayle, S. C. Parker and D. C. Sayle, *Phys. Chem. Chem. Phys.*, 2005, **7**, 2936-2941.
32. Y. G. Wang, D. H. Mei, J. Li and R. Rousseau, *J. Phys. Chem. C*, 2013, **117**, 23082-23089.
33. M. B. Watkins, A. S. Foster and A. L. Shluger, *J. Phys. Chem. C*, 2007, **111**, 15337-15341.
34. D. Marrocchelli and B. Yildiz, *J. Phys. Chem. C*, 2012, **116**, 2411-2424.
35. M. Molinari, S. C. Parker, D. C. Sayle and M. S. Islam, *J. Phys. Chem. C*, 2012, **116**, 7073-7082.
36. S. Gritschneder and M. Reichling, *Nanotechnology*, 2007, **18**, 044024.
37. K. Mudiyanselage, S. D. Senanayake, L. Feria, S. Kundu, A. E. Baber, J. Graciani, A. B. Vidal, S. Agnoli, J. Evans, R. Chang, S. Axnanda, Z. Liu, J. F. Sanz, P. Liu, J. A. Rodriguez and D. J. Stacchiola, *Angew. Chem. Int. Ed.*, 2013, **52**, 5101-5105.
38. T. Bunluesin, H. Cordatos and R. J. Gorte, *J. Catal.*, 1995, **157**, 222-226.
39. G. S. Zafiris and R. J. Gorte, *J. Catal.*, 1993, **143**, 86-91.
40. W. C. Chueh, Y. Hao, W. Jung and S. M. Haile, *Nat. Mater.*, 2012, **11**, 155-161.
41. Z. L. Wu, M. J. Li and S. H. Overbury, *J. Catal.*, 2012, **285**, 61-73.
42. W. Lai and S. M. Haile, *J. Am. Ceram. Soc.*, 2005, **88**, 2979-2997.
43. C. Lu, W. L. Worrell, J. M. Vohs and R. J. Gorte, *J. Electrochem. Soc.*, 2003, **150**, A1357-A1359.
44. C. J. Zhang, M. E. Grass, A. H. McDaniel, S. C. DeCaluwe, F. El Gabaly, Z. Liu, K. F. McCarty, R. L. Farrow, M. A. Linne, Z. Hussain, G. S. Jackson, H. Bluhm and B. W. Eichhorn, *Nat. Mater.*, 2010, **9**, 944-949.
45. W. C. Chueh, W. Lai and S. M. Haile, *Solid State Ionics*, 2008, **179**, 1036-1041.

46. R. D. Green, C. C. Liu and S. B. Adler, *Solid State Ionics*, 2008, **179**, 647-660.
47. S. D. Ebbesen and M. Mogensen, *J. Power Sources*, 2009, **193**, 349-358.
48. K. Mudiyanselage, H. Y. Kim, S. D. Senanayake, A. E. Baber, P. Liu and D. Stacchiola, *Phys. Chem. Chem. Phys.*, 2013, **15**, 15856-15862.
49. A. Hauch, S. D. Ebbesen, S. H. Jensen and M. Mogensen, *J. Mater. Chem.*, 2008, **18**, 2331-2340.
50. V. Yurkiv, D. Starukhin, H. R. Volpp and W. G. Bessler, *J. Electrochem. Soc.*, 2011, **158**, B5-B10.
51. C. J. Zhang, M. E. Grass, Y. Yu, K. J. Gaskell, S. C. DeCaluwe, R. Chang, G. S. Jackson, Z. Hussain, H. Bluhm, B. W. Eichhorn and Z. Liu, *ACS Catal.*, 2012, **2**, 2297-2304.
52. C. J. Zhang, Y. Yu, M. E. Grass, C. Dejoie, W. C. Ding, K. Gaskell, N. Jabeen, Y. P. Hong, A. Shayorskiy, H. Bluhrn, W. X. Li, G. S. Jackson, Z. Hussain, Z. Liu and B. W. Eichhorn, *J. Am. Chem. Soc.*, 2013, **135**, 11572-11579.
53. Z. A. Feng, F. El Gabaly, X. Ye, Z.-X. Shen and W. C. Chueh, *Nat. Commun.*, 2014, **5**, 4374.
54. S. Sharma and M. S. Hegde, *J. Chem. Phys.*, 2009, **130**, 114706.
55. S. Sharma, B. D. Mukri and M. S. Hegde, *Dalton Trans.*, 2011, **40**, 11480-11489.
56. Y. Yu, B. Mao, A. Geller, R. Chang, K. Gaskell, Z. Liu and B. W. Eichhorn, *Phys. Chem. Chem. Phys.*, 2014, **16**, 11633-11639.
57. J. D. Kirtley, D. M. Halat, M. D. McIntyre, B. C. Eigenbrodt and R. A. Walker, *Anal. Chem.*, 2012, **84**, 9745-9753.
58. V. Duboviks, R. C. Maher, M. Kishimoto, L. F. Cohen, N. P. Brandon and G. J. Offer, *Phys. Chem. Chem. Phys.*, 2014, **16**, 13063-13068.
59. F. El Gabaly, A. H. McDaniel, M. Grass, W. C. Chueh, H. Bluhm, Z. Liu and K. F. McCarty, *Chem. Commun.*, 2012, **48**, 8338-8340.
60. T. Staudt, Y. Lykhach, N. Tsud, T. Skala, K. C. Prince, V. Matolin and J. Libuda, *J. Phys. Chem. C*, 2011, **115**, 8716-8724.
61. X. Y. Deng, A. Verdaguer, T. Herranz, C. Weis, H. Bluhm and M. Salmeron, *Langmuir*, 2008, **24**, 9474-9478.
62. H. L. Tuller and A. S. Nowick, *J. Phys. Chem. Solids*, 1977, **38**, 859-867.
63. M. V. Ganduglia-Pirovano, J. L. F. Da Silva and J. Sauer, *Phys. Rev. Lett.*, 2009, **102**, 026101.
64. W. C. Chueh, A. H. McDaniel, M. E. Grass, Y. Hao, N. Jabeen, Z. Liu, S. M. Haile, K. F. McCarty, H. Bluhm and F. El Gabaly, *Chem. Mater.*, 2012, **24**, 1876-1882.

65. M. Huang and S. Fabris, *J. Phys. Chem. C*, 2008, **112**, 8643-8648.

66. K. R. Hahn, M. Iannuzzi, A. P. Seitsonen and J. Hutter, *J. Phys. Chem. C*, 2013, **117**, 1701-1711.